https://doi.org/10.5194/egusphere-2026-4707
Preprint. Discussion started: 2 September 2026

Tidal state as a source of sampling uncertainty in instantaneous-to-daily scaling of mangrove FAPAR

Demei Zhao [a], Haolin Chen [a], Wenmeijun Wang [a], Wenhao Huang [a], Kangwen Zhu [a*]

[a] *School of Smart City, Chongqing Jiaotong University, Chongqing, 400074, China*

*** Corresponding author:** Kangwen Zhu (zhukangwen@cqjtu.edu.cn)

Abstract: A fixed satellite overpass samples mangrove canopies at different stages of the tidal cycle, but the resulting temporal-scaling uncertainty is rarely quantified. We combined half-hourly eddy-covariance measurements from the Qinglangang Mangrove Reserve with harmonically reconstructed water levels to test whether tidal state covaried with an apparent FAPAR proxy and could bias its representation at overpass time. The proxy was 9.8% higher during exposed than flooded periods, and changepoint analysis located a site-specific transition near −0.3 m relative to mean sea level. A post-changepoint sensitivity analysis based on state-specific light-use-efficiency estimates had a coefficient of variation of 3.7%, suggesting that calibration choice alone was unlikely to explain the contrast; however, the proxy was not an independent optical measurement of FAPAR. Across 163 valid days, the median instantaneous-to-daily ratio was 0.83, and applying this site-calibrated ratio reduced in-sample RMSE by 28% relative to a unity-ratio baseline. Sentinel-2 imagery showed directionally compatible spatial patterns, but elevation uncertainty and spatial autocorrelation limited inference. The analysis identifies tidal phase as a source of sampling uncertainty rather than demonstrating a transferable tide-conditioned correction. Testing such a correction will require optical FAPAR, measured water levels, temporally independent evaluation, and

https://doi.org/10.5194/egusphere-2026-4707
Preprint. Discussion started: 2 September 2026

additional mangrove sites.

Keywords: Mangrove forest monitoring; Eddy covariance; Apparent FAPAR; Tidal inundation; Temporal upscaling

1. Introduction

Mangrove forests combine high carbon-storage capacity with direct exposure to tidal forcing (Rani et al., 2023). Reliable monitoring of their canopy function is consequently important for forest conservation, restoration assessment, and blue-carbon accounting (Friess et al., 2019). Satellite gross primary productivity (GPP) products provide regional coverage, but their accuracy depends on the fraction of photosynthetically active radiation absorbed by vegetation (FAPAR). A recent global synthesis for 1996–2020 identified FAPAR as a major predictor of mangrove GPP (Sun et al., 2024), while multi-year eddy-covariance observations show that meteorological and tidal drivers jointly regulate mangrove carbon exchange (Gou et al., 2023). An unresolved monitoring problem is therefore whether an observation acquired at a fixed satellite overpass time represents canopy function consistently when tidal phase changes independently of the solar cycle.

Light-use-efficiency (LUE) models express canopy GPP as the product of FAPAR and an efficiency scalar and are widely used to translate satellite reflectance into productivity estimates (Pei et al., 2022; Zheng & Takeuchi, 2022). Their temporal scaling commonly relies on solar geometry, although a single overpass may not represent the daytime mean. Diffuse radiation penetrates canopy gaps more evenly than direct radiation and can increase whole-canopy quantum yield by reducing local light

https://doi.org/10.5194/egusphere-2026-4707
Preprint. Discussion started: 2 September 2026

saturation (Chakraborty et al., 2022). Clearness-index models therefore separate direct and diffuse radiation when modelling canopy photosynthesis (Spitters et al., 1986). In monsoon mangroves, this radiation effect varies alongside vapour pressure deficit; net ecosystem production at three subtropical sites declined above 2.50–2.95 kPa (Gou et al., 2024). Solar geometry, radiation quality, and atmospheric demand can thus generate within-day variation before tidal effects are considered.

Satellite overpass times are fixed by orbital mechanics, whereas tidal phase follows a separate lunar cycle. The same mangrove stand may therefore be observed with its aerial-root and lower-stem layer exposed or inundated, changing both the background presented to an optical sensor and the environmental conditions under which carbon exchange occurs. Eddy-covariance studies show that tidal and sea-breeze interactions affect net ecosystem exchange (Zhu et al., 2021a), tidal energy advection alters surface-energy partitioning (Yong et al., 2024), salinity modifies the coupling between light absorption and carbon assimilation (Zhu et al., 2021b), and tidal pumping contributes to sub-daily carbon-flux variability (Zhu et al., 2024). These findings establish a process basis for tidal effects, but they do not show whether tidal phase introduces a systematic error when an instantaneous canopy-function proxy is scaled to a daily value. Resolving that distinction is important for forest monitoring: a repeatable sampling bias should be corrected or flagged, whereas a site-specific ecological response should not be generalized as a universal satellite algorithm.

UAV-LiDAR mapping has revealed that the relationship between forest structure and tidal inundation is spatially heterogeneous at the sub-canopy scale (Shih et al.,

https://doi.org/10.5194/egusphere-2026-4707
Preprint. Discussion started: 2 September 2026

2023), and sun-induced chlorophyll fluorescence shows early promise as a remote indicator of canopy photosynthetic capacity sensitive to salinity and tidal stress (Zhu et al., 2021c). Extending tower-derived relationships to satellite pixels requires confronting two sources of spatial uncertainty. Pixel-level observations in raster products are not statistically independent: significance tests applied to full-resolution imagery inflate the apparent number of degrees of freedom unless effective sample size is corrected for spatial autocorrelation (Meyer & Pebesma, 2021). The SRTM digital elevation model, widely used to delineate tidal inundation zones, carries a nominal vertical error of ±5 m (Rodríguez et al., 2006), potentially exceeding the width of intertidal sensitivity zones by nearly an order of magnitude; DEM-based spatial classifications therefore require formal Monte Carlo error propagation before area estimates can be reported with confidence.

We used three safeguards to keep the tidal analysis separate from construction of the response. Tidal height was reconstructed independently of the flux-derived proxy. Maximum light-use efficiency was first calibrated without tidal classes, and class-specific estimates were introduced only as a post-changepoint sensitivity analysis. Tower time series and satellite imagery were also treated as different lines of evidence because MODIS composites and three Sentinel-2 scenes could not validate a sub-daily process independently. Changepoint analysis located an empirical transition without fixing its elevation in advance (Killick et al., 2012), while spatial-autocorrelation diagnostics and DEM error propagation limited the weight assigned to nominal pixel counts (Meyer & Pebesma, 2021).

https://doi.org/10.5194/egusphere-2026-4707
Preprint. Discussion started: 2 September 2026

Here, we combine half-hourly eddy-covariance flux records from the Qinglangang Mangrove Reserve with harmonically reconstructed tidal stages, MODIS FAPAR, Sentinel-2 imagery, and Monte Carlo error propagation to (i) test whether tidal state covaries with the tower-derived apparent FAPAR proxy after keeping the primary efficiency calibration independent of tidal class, (ii) quantify the error from treating the nominal satellite-overpass value as the daytime mean and determine whether the tidal relationship follows a continuous gradient or a site-specific threshold, and (iii) assess whether reserve-wide satellite patterns are directionally compatible with the tower result after accounting for spatial autocorrelation and DEM uncertainty. This design evaluates tidal sampling risk and a site-calibrated scaling ratio; it does not constitute an independently validated tide-conditioned correction.

2. Materials and Methods

We used a four-stage workflow. Quality-controlled eddy-covariance GPP and radiation observations first yielded a half-hourly apparent FAPAR proxy. Tidal elevation was reconstructed independently, and changepoint analysis was used to locate a shift in that proxy. The nominal overpass value was then compared with the daytime mean to quantify temporal-scaling error. MODIS and Sentinel-2 products provided benchmarks for seasonal magnitude and spatial pattern, respectively. Tidal classification diagnosed a potential source of sampling error but did not enter the constant median scaling ratio directly. Because the datasets differed in temporal support and footprint, agreement among them was interpreted as corroboration rather than independent validation.

https://doi.org/10.5194/egusphere-2026-4707
Preprint. Discussion started: 2 September 2026

2.1 Study design and site context

The Qinglangang Mangrove Reserve (19.615° N, 110.798° E) occupies the northeast coast of Hainan Island, China (Fig. 1). Its tropical-monsoon climate and irregular diurnal tide provide a natural test bed in which solar and tidal cycles vary independently. The wet season (May–October) delivers approximately 80% of annual precipitation and has a mean air temperature of 28.2°C; the dry season (November–April) has a mean of 22.5°C. The reserve comprises mature mangrove stands intersected by tidal creeks and channels. Dominant taxa within the tower fetch are Rhizophora stylosa, Bruguiera gymnorrhiza, Kandelia obovata, and Avicennia marina. Mean canopy height is 6.0 m; displacement height (4.02 m) and roughness length (0.90 m) were estimated from the eddy-covariance wind profile. Mean spring and neap tidal ranges are approximately 1.5 and 0.5 m, respectively. The tower location was selected so that the 80% cumulative fetch (approximately 300 m) remained within mangrove canopy for the dominant southeasterly summer and northeasterly winter wind sectors. This configuration reduced land-cover mixing in the tower signal while retaining the full local inundation cycle.

https://doi.org/10.5194/egusphere-2026-4707
Preprint. Discussion started: 2 September 2026

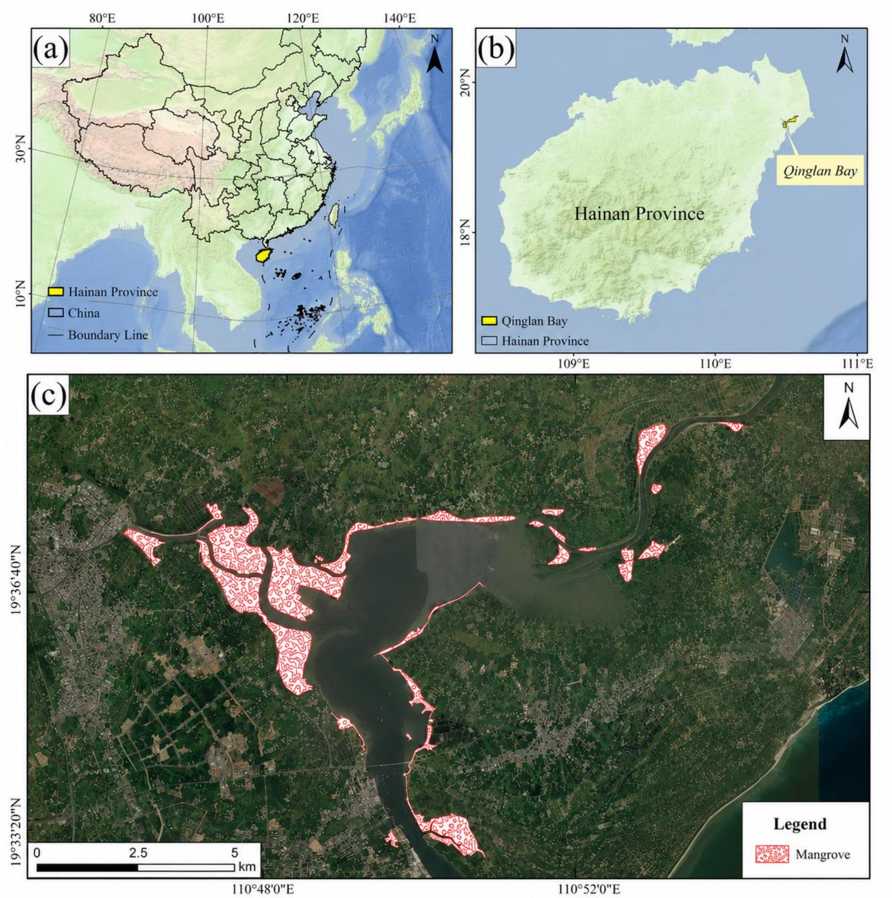

Fig. 1. Geographic setting and mangrove distribution of the study area in Qinglan Bay, Hainan Province, China. (a) Geographic location of Hainan Province in China. (b) Location of Qinglan Bay within Hainan Province. (c) Spatial distribution of mangrove forests in Qinglan Bay derived from imagery. Basemap data in panels (a) and (b) © Resource and Environment Science and Data Center, Chinese Academy of Sciences (RESDC). Satellite imagery in panel (c) © 2026 Google Earth.

2.2 Eddy covariance system and flux data processing

An open-path eddy-covariance (EC) system operated 18.5 m above the sediment surface from 8 March to 9 October 2023, yielding 10,298 half-hourly intervals over 215

https://doi.org/10.5194/egusphere-2026-4707
Preprint. Discussion started: 2 September 2026

days. Three-dimensional wind and sonic temperature were measured at 10 Hz with a Gill WindMaster Pro, and CO_2/H_2O densities were measured at 10 Hz with a LI-COR LI-7500DS. Photosynthetic photon flux density (PPFD; μmol m^{-2} s^{-1}) was recorded with a co-located LI-COR LI-190R quantum sensor. Raw data were processed in EddyPro v7.0 using despiking, double rotation, block averaging, time-lag compensation, Webb–Pearman–Leuning density correction, and high-frequency spectral correction (Webb et al., 1980; Wilczak et al., 2001; Moncrieff et al., 1997, 2004; Mauder et al., 2013; Fratini & Mauder, 2014). Net ecosystem exchange (NEE) was calculated as turbulent CO_2 flux plus storage flux. Intervals with SSITC quality flags ≥2 or more than 100 CO_2 spikes were removed before partitioning. Reporting the acquisition period, instrument heights, frequencies, corrections, and exclusion criteria defines the measurement domain to which subsequent FAPAR inference applies.

NEE was partitioned into gross primary production (GPP) and ecosystem respiration (Reco) in R v4.3 using REddyProc (Wutzler et al., 2018). Atmospheric turbulence sufficiency was assessed by the friction-velocity (u*) threshold method of Papale et al. (2006); records below the site-specific threshold were excluded. Gaps were filled by the marginal distribution sampling algorithm (Reichstein et al., 2005). Nighttime Reco was parameterized using the Lloyd–Taylor (1994) equation fitted in 15-day moving windows to quality-controlled nocturnal NEE (PPFD < 20 μmol m−2 s−1):

$$R_{eco} = R_{(ref)}\exp\left(E_{0}\left(\frac{1}{T_{ref}-T_{0}}-\frac{1}{T_{a}-T_{0}}\right)\right) \quad (1)$$

where R_{ref} (μmol CO_2 m^{-2} s^{-1}) and E_0 (K) were estimated by non-linear least squares

https://doi.org/10.5194/egusphere-2026-4707
Preprint. Discussion started: 2 September 2026

within each window. Daytime R_{eco} was extrapolated from (1), and GPP was obtained as:

$$GPP = R_{eco} - NEE \quad (2)$$

GPP was set to zero at night. The attrition sequence was retained explicitly: of 10,298 initial half-hourly intervals, 3,847 daytime records met PPFD >20 µmol m^{-2} s^{-1} after flux processing; excluding Kt <0.05 and physically inadmissible apparent-FAPAR estimates left 3,137 intervals for analysis. This transparent flow separates losses caused by flux quality control, the daytime definition, radiation screening, and inversion bounds. Daily summaries were calculated only for days with at least 20 valid daytime intervals, reducing sensitivity to uneven within-day coverage.

2.3 Environmental, radiation, and tidal data

Half-hourly meteorological variables recorded at the tower included air temperature (T_a; °C) and relative humidity (RH; %) from a Vaisala HMP155 probe at 18.5 m; precipitation from a TE525MM tipping-bucket gauge; and soil temperature and volumetric water content from CS655 sensors (Campbell Scientific) at 5 cm depth. Vapour pressure deficit (VPD; hPa) was derived from T_a and RH. Downwelling global solar radiation (R_g; W m^{-2}) was measured by a Kipp & Zonen CMP6 pyranometer co-located with the tower. The clearness index was computed as:

$$K_t = \frac{R_g}{R_0} \quad (3)$$

where R0 is extraterrestrial irradiance on a horizontal surface, computed from site coordinates, day-of-year, and local time using standard solar geometry (Gueymard, 2008). The diffuse fraction of incoming radiation was estimated from Kt using the

https://doi.org/10.5194/egusphere-2026-4707
Preprint. Discussion started: 2 September 2026

piecewise empirical model of Spitters et al. (1986). Records with Kt < 0.05 were excluded from all FAPAR and DF analyses to avoid physically unreliable diffuse-fraction estimates under near-opaque cloud.

Half-hourly tidal water levels at the tower coordinates were reconstructed from the FES2014 global ocean tide atlas (Lyard et al., 2021) by summing contributions of 11 dominant constituents for the South China Sea region using the UTide package. Hourly predictions were linearly interpolated to 30-min resolution to produce a continuous tidal height record $h(t)$.

2.4 Tide-robust retrieval of an apparent FAPAR proxy

At each valid half-hour, an apparent canopy FAPAR proxy was derived by rearranging the Monteith light-use-efficiency framework (Monteith, 1972, 1977). The proxy linked observed GPP to incident PPFD through a season-specific maximum-efficiency term and was used to test temporal covariation with tidal state. We refer to it as 'apparent' FAPAR because EC observations constrain the product of absorbed radiation and realized efficiency rather than measuring optical absorption independently.

$$FAPAR_{inst}(t) = \frac{GPP(t)}{\varepsilon_{max} PPFD(t)} \quad (4)$$

GPP and PPFD are expressed in μmol CO_2 m^{-2} s^{-1} and μmol photons m^{-2} s^{-1}, respectively, so the derived proxy is dimensionless. To prevent tidal classification from determining the quantity later tested against tide, the primary εmax calibration pooled tidal states within each season and used only high-irradiance, clear-sky intervals (PPFD >800 μmol m^{-2} s^{-1}; Kt >0.6). After the changepoint had been estimated, εmax was recalibrated separately by tidal class as a sensitivity analysis; its coefficient of

https://doi.org/10.5194/egusphere-2026-4707
Preprint. Discussion started: 2 September 2026

variation quantified how strongly the inferred tidal contrast depended on the efficiency calibration. This sequence was intended to reduce circularity between tidal grouping and FAPAR inversion. It did not make the proxy equivalent to an independent optical FAPAR measurement, so satellite FPAR was used only as an external magnitude benchmark.

2.5 Data-driven threshold detection and tidal classification

To distinguish a threshold-like response from a continuous gradient without pre-specifying its elevation, the apparent FAPAR observations were ordered by independently reconstructed tidal height and analyzed with the PELT changepoint algorithm using a radial-basis-function cost. The tidal series was generated without using GPP, PPFD, or FAPAR, preserving separation between the candidate driver and the response. Because adjacent half-hours and neighbouring tidal elevations are not independent replicates, the changepoint was interpreted as a site-level structural estimate rather than a universal population threshold.

$$\sum C\left(y_{\tau_{i-1}+1:\tau_i}\right) + \beta m \tag{5}$$

Here, m is the number of changepoints, τi their ordered locations, C (·) is the segment cost, and β is the modified-BIC penalty (Zhang & Siegmund, 2007). The detected breakpoint was examined using piecewise linear fits above and below the candidate elevation. Robustness was evaluated by stepping candidate thresholds from −0.5 to +0.5 m MSL in 0.1-m increments and by checking whether the direction of the exposed–flooded contrast was retained across seasons. These analyses were used to assess threshold stability; they did not substitute for independent replication at another site or

https://doi.org/10.5194/egusphere-2026-4707
Preprint. Discussion started: 2 September 2026

year.

Only after threshold estimation were intervals classified as exposed [h(t) < hc] or flooded [h(t) ≥ hc]. The ±0.3 m band around hc was defined as a spatial sensitivity zone to accommodate unresolved microtopographic variability; it was not treated as a precisely mapped ecological boundary. Exposed–flooded comparisons used Kruskal–Wallis and Bonferroni-adjusted Mann–Whitney tests, with effect magnitude and seasonal consistency considered alongside p values. Given serial dependence among half-hourly intervals, these tests characterized within-record separation and were not interpreted as replication across independent ecosystems.

2.6 Instantaneous-to-daily scaling and tidal diagnostics

The instantaneous-to-daily FAPAR upscaling ratio was defined as:

$$R_{FAPAR} = \frac{FAPAR_{(inst)(t_{overpass})}}{(FAPAR)_{daily}} \tag{6}$$

where $FAPAR_{inst}(t_{overpass})$ is the tower-derived FAPAR at the Sentinel-2 overpass time (10:30 LST) and $\overline{FAPAR}_{daily}$ is the daytime-mean FAPAR for that calendar day; R_{FAPAR} is dimensionless. The analogous GPP upscaling ratio is:

$$R_{GPP} = \frac{GPP(t_{overpass})}{(GPP)_{daily}} \tag{7}$$

Two operational strategies were compared. The unity-ratio baseline assumed that FAPAR at 10:30 LST equalled the daytime mean. The site-calibrated strategy used the median ratio across valid days, with the daily mean recovered by applying the inverse of the defined instantaneous-to-daily ratio. The median was chosen before model comparison because it is less sensitive than the mean to days with short-term cloud or flux anomalies. Tidal class was analysed as a potential source of variation around this

https://doi.org/10.5194/egusphere-2026-4707
Preprint. Discussion started: 2 September 2026

scaling relationship but was not included as a predictor in the constant-ratio calibration. The analogous GPP ratio was retained as a process comparison rather than used to redefine FAPAR.

$$\overline{FAPAR}_{daily}^{cal} = \frac{FAPAR_{(inst)(t_{overpass})}}{\tilde{\mathrm{R}}_{FAPAR}} \tag{8}$$

Performance was summarized by RMSE against observed daytime means for 163 valid days and compared with the unity-ratio baseline. The same single-site record supplied both the median ratio and the evaluation days, so the reduction in error measured internal calibration performance rather than out-of-sample prediction. A ridge model (Hoerl & Kennard, 1970) was fitted as an exploratory test of whether the available covariates added information beyond the constant median. Neither the constant ratio nor the ridge model was evaluated with temporally blocked or external data; transferability was therefore not assessed.

2.7 Cross-platform benchmarking and scale-aware spatial analysis

MODIS MOD15A2H v061 FPAR/LAI (500 m, 8-day composites; Knyazikhin et al., 1998; Myneni et al., 2021) was obtained for March–November 2023, reprojected to WGS84, and clipped to the reserve. Twenty-seven tower–MODIS windows were matched at the tower footprint to test seasonal magnitude agreement between methodologically distinct retrievals. Tidal state at the nominal Terra overpass time was assigned from the reconstructed water level, but the 8-day composite was not treated as an instantaneous observation. Consequently, the tidal-class comparison was explicitly exploratory: a null contrast may reflect compositing, footprint mixing, retrieval uncertainty, or limited class counts.

https://doi.org/10.5194/egusphere-2026-4707
Preprint. Discussion started: 2 September 2026

Three cloud-limited Sentinel-2 Level-2A scenes (March, July, and October 2023; 10 m; reported cloud cover <10%) were processed with the SNAP biophysical processor, which retrieves FAPAR through a PROSAIL-trained neural network (Jacquemoud et al., 2009). Vegetated, cloud-free pixels with NDVI >0.3 were retained. Sentinel-2 provided spatial pattern information at higher resolution, but only three seasonal snapshots; it was therefore used to examine directional consistency with the tower threshold rather than to estimate a temporally general tidal effect.

SRTM 30-m DEM tiles were bilinearly resampled to the 10-m Sentinel-2 grid. Using the changepoint elevation h_c identified in §2.5, pixels were assigned to three zones: elevated (DEM > $h_c + 0.3$ m), tidal-FAPAR sensitive ($h_c - 0.3$ m to $h_c + 0.3$ m), and low-lying (DEM < $h_c - 0.3$ m). Spatial autocorrelation of Sentinel-2 FAPAR was quantified by fitting an exponential semivariogram model:

$$\gamma(d) = c_0 + c_{1\left(1-exp\left(-\frac{d}{a}\right)\right)} \tag{9}$$

using the 'gstat' R package (Pebesma, 2004). The decorrelation distance d_{corr} equals the range parameter a. The effective number of spatially independent samples within the reserve was estimated as:

$$N_{eff} \approx \frac{A}{\pi d_{corr}^2} \tag{10}$$

When Neff was substantially smaller than the pixel count, formal pixel-level significance testing was not performed; the Sentinel-2 spatial patterns were instead reported as qualitative consistency checks.

SRTM's nominal ±5 m vertical uncertainty exceeds the 0.6 m sensitivity-zone width. A Monte Carlo propagation was therefore used to report a distribution and 95%

https://doi.org/10.5194/egusphere-2026-4707
Preprint. Discussion started: 2 September 2026

interval for the detectable zone fraction rather than an unqualified area estimate. This analysis quantified classification sensitivity to DEM error; it could not recover sub-metre elevation information absents from SRTM.

2.8 Exploratory spatial associations and statistical safeguards

Random forests were used only to describe multivariate associations with scene-specific Sentinel-2 FAPAR. Six candidate predictors were examined: atmospheric CO_2, solar radiation, precipitation, land-surface temperature, PAR, and SRTM elevation. Models used 500 trees implemented with ranger (Wright & Ziegler, 2017) and were summarized by out-of-bag R^2 and SHAP values (Lundberg & Lee, 2017). NASA POWER meteorological variables have 0.5° resolution and therefore provide broad scene-level context rather than independent 10-m variation within the reserve. SHAP rankings were interpreted as properties of the fitted FAPAR models under correlated and scale-mismatched predictors, not as causal partitions, spatially independent validation, or pixel-scale environmental effects.

Statistical interpretation followed the sampling support of each dataset. Non-parametric group comparisons were used for skewed tower-derived quantities, with exact sample sizes and effect magnitudes reported alongside p values. Calendar days, rather than half-hours, were the support for upscaling performance. For Sentinel-2, an exponential semivariogram was used to estimate decorrelation distance and effective sample size; nominal pixel counts were not treated as independent replication. Cross-sensor comparisons used matched temporal windows, while differences in footprint and compositing were carried into interpretation. This hierarchy prevents large half-hourly

https://doi.org/10.5194/egusphere-2026-4707
Preprint. Discussion started: 2 September 2026

or pixel counts from generating spurious precision and keeps confirmatory, sensitivity, and exploratory analyses distinct.

All analyses were organized around three levels of evidence. Half-hourly tower observations supported process-level and changepoint analyses; calendar days were the units for instantaneous-to-daily scaling; and effective, rather than nominal, pixel counts governed interpretation of spatial imagery. Results derived from the same record used for calibration were labelled internal or exploratory. Parameters, thresholds, exclusion rules, software versions, and sample attrition were reported to facilitate reproduction. This organization separated estimation, sensitivity analysis, and external benchmarking and avoided treating agreement among non-independent analyses as independent validation.

3. Results

3.1 Seasonal diurnal GPP and environmental context

Half-hourly GPP varied seasonally in both magnitude and diurnal shape (Fig. 2). The midday peak increased from approximately 12 µmol m^{-2} s^{-1} in March to 18 µmol m^{-2} s^{-1} in July and then declined through October. The diurnal envelope was narrowest in March and broadest in July–August. Monthly GPP amplitude covaried with day length ($r = 0.89$), consistent with a strong seasonal influence of solar geometry. Tidal differences in the apparent FAPAR proxy were examined against this seasonal background.

https://doi.org/10.5194/egusphere-2026-4707
Preprint. Discussion started: 2 September 2026

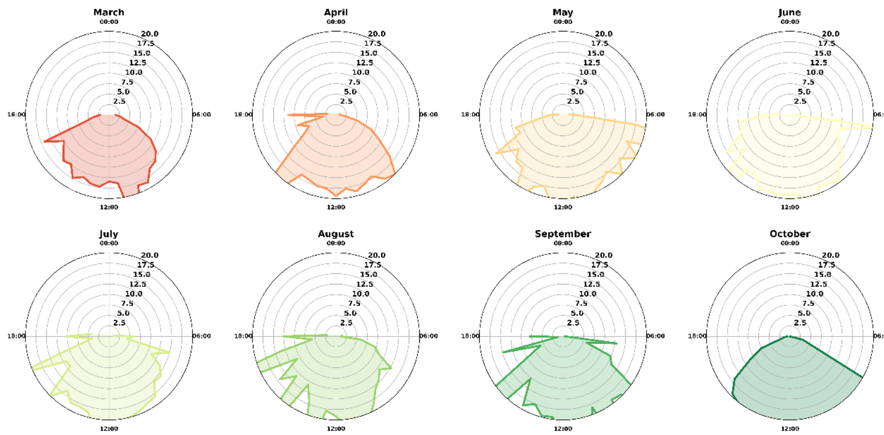

Fig. 2. Monthly diurnal GPP patterns. Polar coordinates: angle represents time of day, radius represents mean half-hourly GPP (μmol m^{-2} s^{-1}). The midday GPP peak strengthens from March to July and contracts by October, reflecting seasonal variation in photoperiod and photosynthetic capacity.

Several environmental variables differed between tidal states (Fig. 3). Exposed periods had higher water-use efficiency than flooded periods (Kruskal–Wallis $p < 0.05$; Fig. 3a). The H/LE ratio was also higher during flooding (Fig. 3b), while friction velocity declined weakly with tidal height (Fig. 3c). Near-surface CO_2 concentration and the Bowen ratio were higher during flooded intervals (Fig. 3d,e). Diffuse radiation followed similar diurnal courses in the two tidal classes (Fig. 3f). These comparisons describe covariation within the tower record; they do not by themselves identify the processes responsible for the differences.

https://doi.org/10.5194/egusphere-2026-4707
Preprint. Discussion started: 2 September 2026

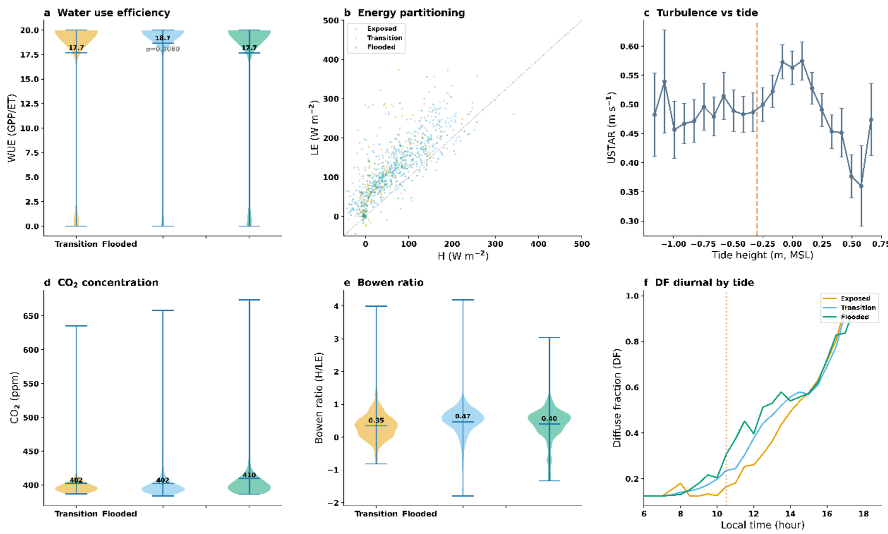

Fig. 3. Environmental responses to tidal state. (a) Water use efficiency (WUE = GPP/ET). (b) Energy partitioning (H vs LE) colored by tidal state. (c) Friction velocity (USTAR) as a function of continuous tide height; dashed line marks the −0.3 m changepoint. (d) Near-surface CO_2 concentration by tidal state. (e) Bowen ratio (H/LE) by tidal state. (f) Diurnal course of the diffuse fraction (DF) stratified by tidal state.

3.2 Tidal covariation in apparent FAPAR and temporal-scaling error

FAPARinst declined with increasing clearness index (Kt) in all three seasons (Fig. 4a); binned means fell from approximately 0.85 at Kt < 0.3 to approximately 0.65 at Kt > 0.8. FAPARinst also decreased across the observed VPD range (Fig. 4b) but showed little additional response to PPFD above approximately 500 µmol m^{-2} s^{-1} (Fig. 4c). The diffuse-fraction distribution was right-skewed (mean = 0.46, median = 0.27; Fig. 4d), and its relationship with Kt followed the Spitters curve (Fig. 4e). Records with Kt < 0.05, representing 6.9% of daytime observations, were excluded (Fig. 4f). Because the proxy was derived from GPP, PPFD, and calibrated efficiency, its associations with

https://doi.org/10.5194/egusphere-2026-4707
Preprint. Discussion started: 2 September 2026

Kt and VPD could reflect changes in realized light-use efficiency as well as optical absorption.

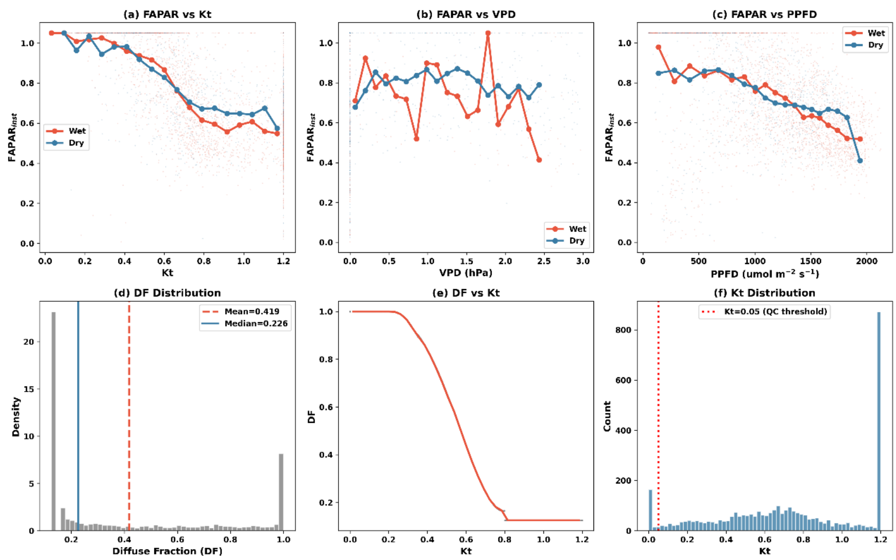

Fig. 4. Environmental associations and radiation diagnostics for FAPARinst. (a–c) FAPARinst in relation to Kt, VPD, and PPFD by season (binned means ± SE). (d) Distribution of diffuse fraction (DF). (e) DF in relation to Kt, with binned mean shown by the solid line. (f) Distribution of Kt; the dashed line indicates the exclusion threshold (Kt < 0.05).

Instantaneous FAPAR at the nominal overpass time was positively associated with the daytime mean (r = 0.76; Fig. 5a). Across 163 valid days, the instantaneous-to-daily ratio had a median of 0.83 (Fig. 5b), so the 10:30 value averaged 83% of the daytime mean. Applying this ratio reduced RMSE by 28% relative to the unity-ratio assumption (Fig. 5c). This was an in-sample improvement because the ratio and its performance were estimated from the same record.

https://doi.org/10.5194/egusphere-2026-4707
Preprint. Discussion started: 2 September 2026

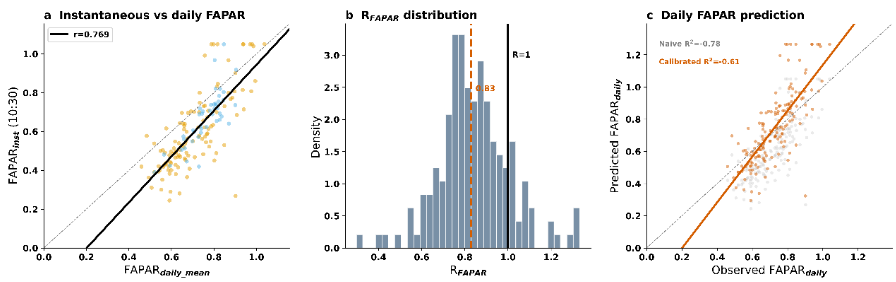

Fig. 5. Instantaneous-to-daily FAPAR upscaling. (a) FAPAR at Sentinel-2 overpass (10:30) versus daytime-mean FAPAR. (b) Distribution of the upscaling ratio R_{FAPAR} = $FAPAR_{inst}$ / $FAPAR_{daily}$mean (median = 0.83). (c) Daily FAPAR predicted by the naive assumption (R = 1, grey) and the calibrated ratio (R = 0.83, orange).

Half-hourly FAPARinst differed between tidal states, with exposed-period values 9.8% higher than flooded-period values (0.780 ± 0.239 vs. 0.711 ± 0.271; Kruskal–Wallis p = 0.0075; Bonferroni-adjusted Mann–Whitney U p = 0.003; Fig. 6a). These p values quantify separation within the serially dependent tower record and do not represent replication across independent ecosystems. The direction of the contrast was consistent across spring, summer, and autumn. State-specific LUE calibration under PPFD > 800 μmol m^{-2} s^{-1} and Kt > 0.6 yielded a coefficient of variation of 3.7% (Fig. 6b), indicating limited sensitivity to the selected calibration while not independently excluding inversion bias. The exposed–flooded separation persisted across daylight hours and was greatest from mid-morning to early afternoon (Fig. 6c). Changepoint detection identified one break at −0.3 m MSL (Fig. 6d). Piecewise fits showed little additional trend on either side, consistent with a threshold-like pattern within this dataset. The interval from −0.6 to 0 m MSL was retained as the site-specific tidal-FAPAR sensitivity zone.

https://doi.org/10.5194/egusphere-2026-4707
Preprint. Discussion started: 2 September 2026

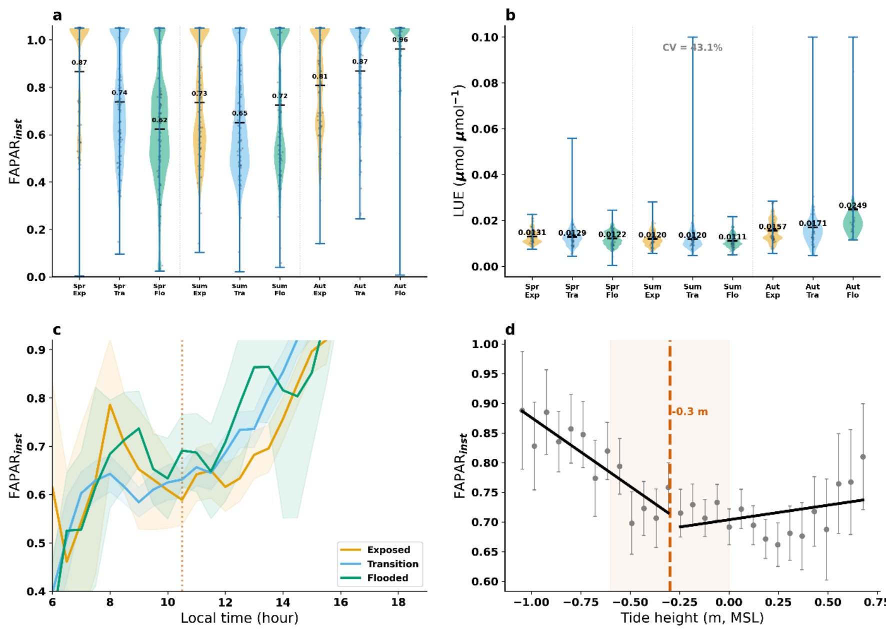

Fig. 6. Tidal modulation of instantaneous FAPAR. (a) $FAPAR_{inst}$ by season and tidal state. (b) LUE under optimal conditions, stratified by season and tidal state (CV = 3.7%). (c) Diurnal $FAPAR_{inst}$ by tidal state (shading: 95% CI). (d) Changepoint detection at −0.3 m MSL; red band: sensitivity zone.

3.3 Cross-platform benchmarking and seasonal stability

Correlation matrices were used to describe the seasonal stability of environmental associations (Fig. 7). GPP correlated most strongly with PPFD (r = 0.65–0.72), followed by Kt (r = 0.45–0.55). The GPP–DF correlation was negative in both seasons and stronger during the wet season (r = −0.38 versus −0.21). Correlations with VPD (r = −0.15 to −0.22) and air temperature (r = 0.18–0.25) were weaker. Kt and DF were strongly negatively correlated (r = −0.72 to −0.78). The rank order of these associations was similar in wet and dry subsets, although their magnitudes differed. These descriptive results supported use of the pooled daytime record but did not establish

https://doi.org/10.5194/egusphere-2026-4707
Preprint. Discussion started: 2 September 2026

causal environmental controls.

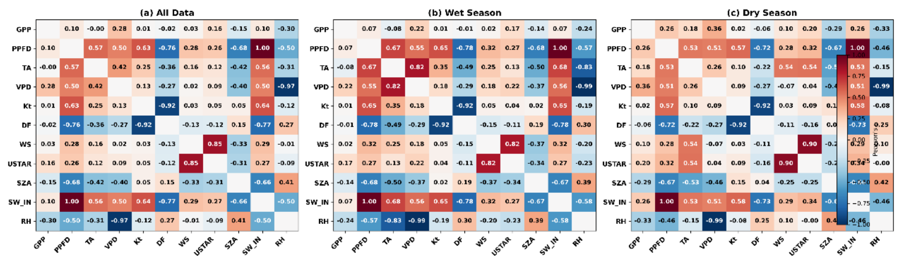

Fig. 7. Variable correlation matrices by season. Pearson correlation coefficients among eleven half-hourly variables for (a) all data, (b) wet season, and (c) dry season. GPP is most strongly correlated with PPFD ($r = 0.65$–0.72) and Kt ($r = 0.45$–0.55). The GPP–DF correlation is negative and stronger in the wet season ($r = -0.38$) than the dry season ($r = -0.21$), consistent with greater cloud–radiation variability during the monsoon

Tower-derived FAPAR and MODIS MOD15A2H FPAR were rank-correlated across 27 matched 8-day windows at the tower pixel (Spearman $\rho = 0.47$, $p = 0.013$; RMSE = 0.095; bias = −0.02; Fig. 8a). Both series declined from March to October (Fig. 8b). The half-hourly tower record retained the 9.8% exposed–flooded contrast reported in Section 3.2, and a representative 3-day interval ranged from 0.63 to 0.98 (Fig. 8c). MODIS composites did not differ detectably among tidal states (Kruskal–Wallis $p = 0.36$); exposed and flooded means were 0.71 ± 0.07 (n = 7) and 0.76 ± 0.04 (n = 5), respectively (Fig. 8f). The MODIS value for 9 March (0.76) was close to the corresponding 3-day tower mean (0.77), but the comparison cannot resolve sub-daily tidal variation.

Stratified by DEM-derived tidal sensitivity zone, wet-season FAPAR was 0.60 ±

https://doi.org/10.5194/egusphere-2026-4707
Preprint. Discussion started: 2 September 2026

0.29 (n = 18) for elevated pixels (> 0 m), 0.71 ± 0.19 (n = 3) for sensitive pixels (−0.6 to 0 m), and 0.59 ± 0.09 (n = 8) for low-lying pixels (< −0.6 m); dry-season values were 0.57 ± 0.28 (*n* = 21), 0.61 ± 0.18 (*n* = 3), and 0.54 ± 0.18 (*n* = 9), respectively (Fig. 8d). Differences among zones were not statistically significant in either season (wet: Kruskal–Wallis *p* = 0.81; dry: *p* = 0.98). The tower-pixel MODIS FAPAR fell within the central mass of the reserve-wide distribution in both seasons (Fig. 8e).

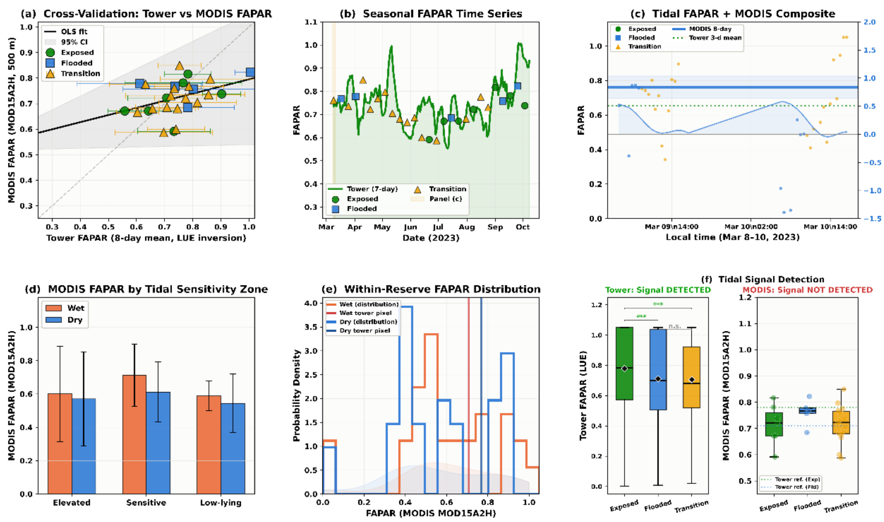

Fig. 8. Comparison of tower-derived and MODIS FAPAR. (a) Tower-derived FAPAR versus MODIS MOD15A2H at the tower pixel, classified by tidal state at nominal overpass. (b) Seasonal series of tower and 8-day MODIS values. (c) Three-day interval (8–10 March) with the coincident MODIS composite. (d) MODIS FAPAR by DEM-derived tidal-sensitivity zone. (e) Reserve-wide distributions with the tower pixel indicated. (f) Tidal-class comparisons for the tower record and MODIS composites.

3.4 Spatial variation of FAPAR across seasons, elevations, and offshore distances

Sentinel-2 FAPAR varied spatially in all three scenes (Fig. 9). Mean values were

https://doi.org/10.5194/egusphere-2026-4707
Preprint. Discussion started: 2 September 2026

0.137 ± 0.111 in spring, 0.193 ± 0.156 in summer, and 0.187 ± 0.139 in autumn, based on 145,649, 144,980, and 138,775 valid pixels, respectively. Pixels above mean sea level had the highest mean FAPAR (0.154–0.218), whereas the DEM-defined sensitivity zone had lower values (0.081–0.116), a difference of 44–48% with Cohen's d ranging from −0.65 to −0.67. Low-lying pixels were intermediate (0.097–0.156). Because pixel values were spatially autocorrelated and elevation was uncertain, these contrasts were treated as descriptive spatial patterns rather than independent tests of tidal effects.

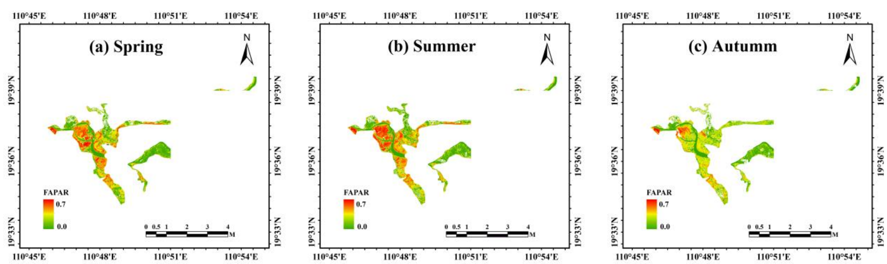

Fig. 9. Seasonal FAPAR spatial maps. Sentinel-2 FAPAR for (a) Spring, (b) Summer, and (c) Autumn.

Binned FAPAR increased with elevation in each Sentinel-2 scene (Fig. 10). Within −2 to +2 m MSL, fitted slopes ranged from 0.008 to 0.012 m^{-1} and descriptive correlations ranged from $r = 0.71$ to 0.79. Values approached 0.25–0.30 above +4 m. FAPAR also increased with distance from mapped tidal channels, from 0.10–0.12 within 20 m to 0.18–0.22 beyond 200 m, although this association was weaker ($r = 0.42$–0.55). Distance to a mapped channel is an imperfect proxy because hydrological connections vary among channels. The elevation and distance patterns were therefore interpreted as spatial context for the tower result, not as confirmation of its mechanism.

https://doi.org/10.5194/egusphere-2026-4707
Preprint. Discussion started: 2 September 2026

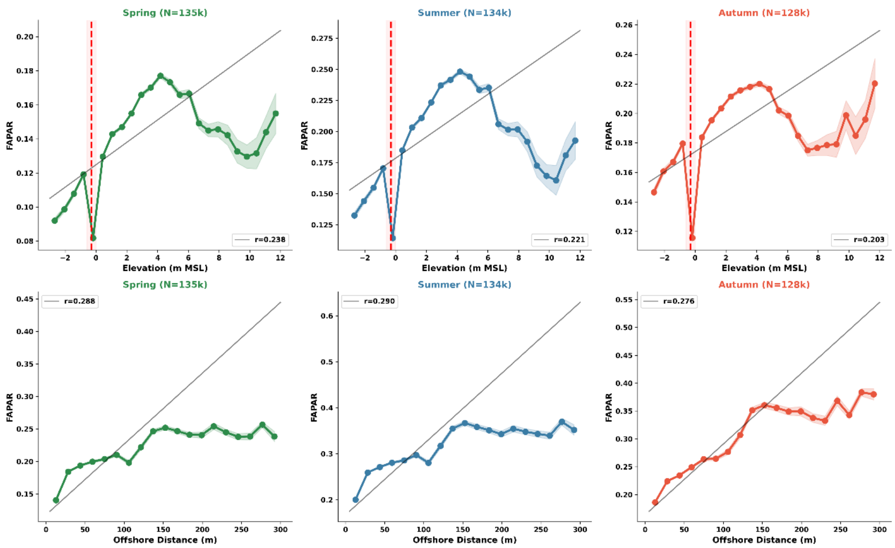

Fig. 10. FAPAR as a function of elevation and offshore distance. Binned means (± SE) of Sentinel-2 FAPAR against (a–c) elevation for Spring, Summer, and Autumn, and (d–f) offshore distance for the same seasons. The red dashed line marks the −0.3 m changepoint; the red band spans the tidal-FAPAR sensitivity zone.

3.5 Exploratory environmental associations with mapped FAPAR

Random-forest models fitted to scene-specific Sentinel-2 FAPAR with six environmental predictors yielded out-of-bag R^2 values of 0.807 in spring, 0.692 in summer, and 0.740 in autumn (Figs. 11–13). These values describe model fit within the sampled imagery; because pixels were spatially autocorrelated and several meteorological predictors were available only at 0.5° resolution, they should not be interpreted as spatially independent predictive performance.

In spring, SHAP importance was 31.7% for CO_2 concentration, 31.3% for solar radiation, 18.8% for precipitation, 8.6% for PAR, 5.1% for land-surface temperature, and 4.4% for elevation (Fig. 11). The fitted FAPAR response was positive at low-to-

https://doi.org/10.5194/egusphere-2026-4707
Preprint. Discussion started: 2 September 2026

moderate CO_2 concentrations and flattened above approximately 410 ppm, while solar radiation showed a positive monotonic association. These patterns describe the fitted model under correlated and scale-mismatched predictors and should not be interpreted as causal effects.

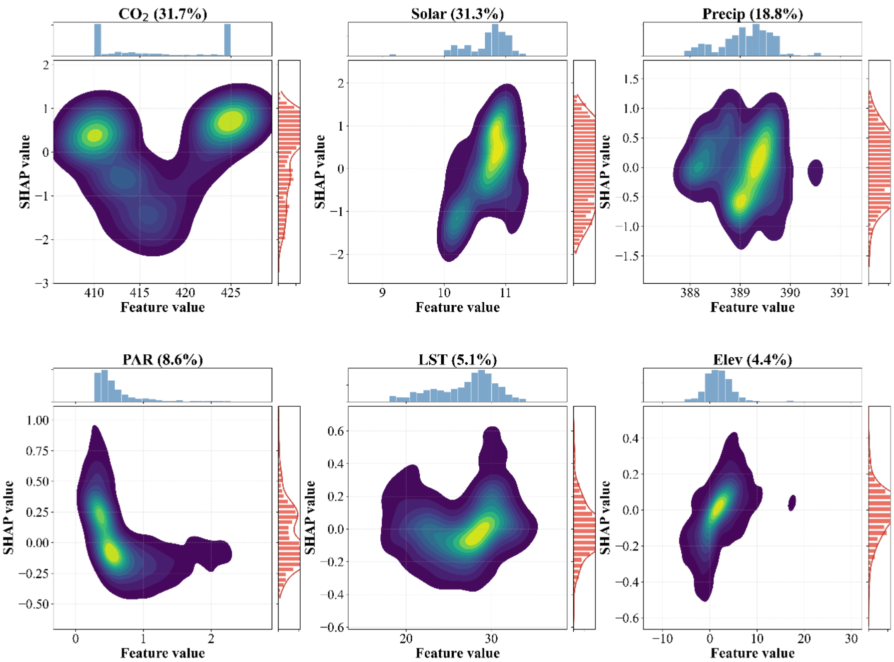

Fig. 11. Exploratory environmental associations with mapped FAPAR in spring. SHAP KDE for six predictors (out-of-bag $R^2 = 0.807$). CO_2 (31.7%) and solar radiation (31.3%) received the largest shares of model importance.

In summer, SHAP importance was 36.0% for CO_2, 19.0% for land-surface temperature, 15.4% for PAR, 10.2% for solar radiation, 9.9% for precipitation, and 9.6% for elevation (Fig. 12). The land-surface-temperature range was 24–38°C, and elevation reached its highest relative contribution among the three scenes. The positive elevation association was directionally consistent with the mapped inundation pattern, but the

https://doi.org/10.5194/egusphere-2026-4707
Preprint. Discussion started: 2 September 2026

model cannot separate elevation effects from correlated spatial structure.

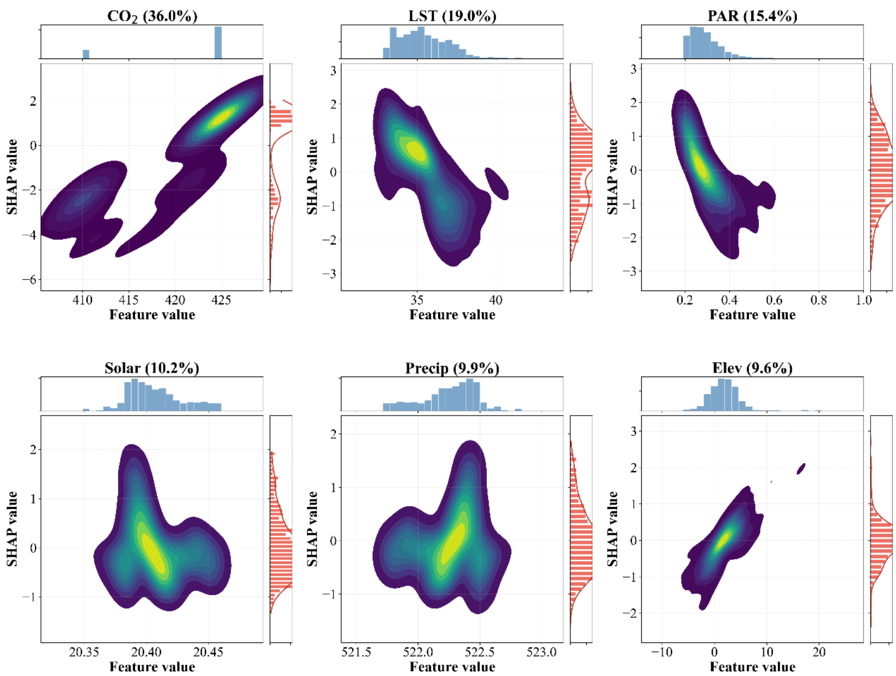

Fig. 12. Exploratory environmental associations with mapped FAPAR in summer. SHAP KDE for six predictors (out-of-bag $R^2 = 0.692$). CO_2 received the largest share of model importance (36.0%), followed by LST (19.0%).

In autumn, SHAP importance was 44.3% for solar radiation, 22.3% for precipitation, 15.6% for CO_2, 10.4% for land-surface temperature, and less than 5% each for PAR and elevation (Fig. 13). The rise in solar-radiation importance from 31.3% in spring to 44.3% in autumn coincided with the seasonal transition toward clearer conditions. Because the coarse meteorological predictors mainly varied between scenes rather than among 10-m pixels, these changes are reported as exploratory model behavior rather than mechanistic attribution.

https://doi.org/10.5194/egusphere-2026-4707
Preprint. Discussion started: 2 September 2026

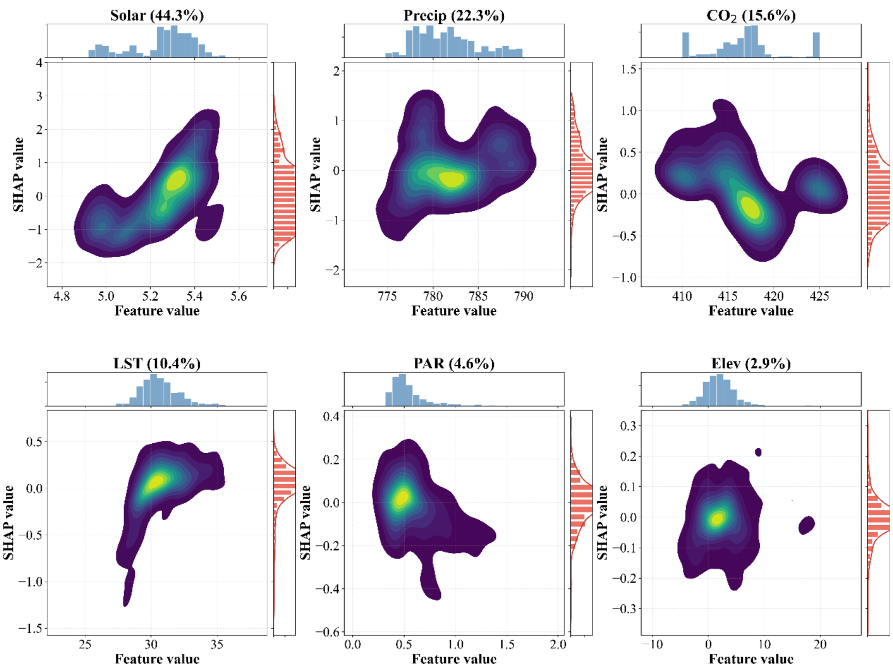

Fig. 13. Exploratory environmental associations with mapped FAPAR in autumn. SHAP KDE for six predictors (out-of-bag R^2 = 0.740). Solar radiation received the largest share of model importance (44.3%), followed by precipitation (22.3%).

Across the three scenes, elevation contributed approximately 3–10% of SHAP importance. Elevation SHAP values were generally positive above approximately 0 m MSL and negative or near zero below this level, directionally matching the tower-derived pattern near −0.3 m MSL. Its contribution remained smaller than those assigned to CO_2, solar radiation, and precipitation. This consistency is descriptive rather than an independent validation because elevation was included directly in the landscape model and both analyses represent the same site.

4. Discussion

4.1 Ecological interpretation of the −0.3 m tidal threshold

https://doi.org/10.5194/egusphere-2026-4707
Preprint. Discussion started: 2 September 2026

Piecewise analysis identified a site-specific break near −0.3 m MSL (Fig. 6d). The apparent FAPAR proxy was 9.8% higher during exposed than flooded intervals, and the direction of this contrast was retained across spring, summer, and autumn. The breakpoint therefore marked a repeatable transition within the tower record rather than a difference confined to one season. Its ecological meaning must nevertheless be kept local: the elevation is referenced to the site datum and may vary with stand structure, microtopography, species composition, and tidal range.

The estimated elevation overlaps the reported vertical range of aerial-root structures in some mangrove taxa (Nguyen et al., 2023), but root height was not measured at the tower footprint. Two non-exclusive processes could contribute. Water may obscure part of the aerial-root and understory stratum, thereby changing the fraction of plant area exposed to incident radiation, while root-zone inundation may alter gas exchange and realized light-use efficiency (Zhu et al., 2021b; Gou et al., 2023). Because the response variable was inferred from GPP and PPFD, the analysis could not separate an optical change from a physiological response. The threshold is consequently compatible with these processes but does not demonstrate either one.

Several diagnostics narrowed the range of alternative explanations. State-specific εmax estimates varied by only 3.7% (Fig. 6b), indicating that the exposed–flooded contrast was not highly sensitive to the efficiency calibration used after changepoint detection. Diffuse fraction showed no clear tidal-state separation (Fig. 3f), whereas water-use efficiency, the H/LE ratio, friction velocity, near-surface CO_2, and the Bowen ratio covaried with tidal state (Fig. 3). These concurrent changes suggest that inundation

https://doi.org/10.5194/egusphere-2026-4707
Preprint. Discussion started: 2 September 2026

was embedded in a broader micrometeorological transition. They also explain why the observed contrast should be described as tidal covariation in apparent FAPAR, rather than as a direct measurement of canopy absorption or a single physiological mechanism.

4.2 Consequences for instantaneous-to-daily scaling

The temporal-scaling analysis showed that the nominal 10:30 overpass did not represent the daytime mean uniformly. Across 163 valid days, the median instantaneous-to-daily FAPAR ratio was 0.83 (Fig. 5b), and applying this empirical ratio reduced RMSE by 28% relative to the unity-ratio baseline (Fig. 5c). The size of the improvement indicates that assuming equality between an instantaneous observation and the daytime mean introduced appreciable error at this site. Because the same record supplied both the ratio and its evaluation, however, the 28% reduction measures internal calibration performance and should not be read as an expected out-of-sample gain.

This reduction was larger than the 7–8% reported for temporal upscaling of MODIS FAPAR across 78 FLUXNET forest sites (Zhang et al., 2023). Differences in canopy structure, sampling time, radiation regime, tidal exposure, and validation design could all contribute to the contrast. The present study cannot assign the difference specifically to tide, but it identifies tidal state as an additional source of within-day variation that is absent from conventional solar-geometry scaling. A fixed overpass may therefore sample not only a particular point on the diurnal radiation curve but also a different hydrological state from one date to another.

Radiation quality provides a second source of variation. Apparent FAPAR declined

https://doi.org/10.5194/egusphere-2026-4707
Preprint. Discussion started: 2 September 2026

with increasing clearness index and VPD (Fig. 4), and diffuse fraction was retained in the exploratory ridge model of the scaling ratio. These patterns are consistent with the known influence of diffuse radiation and atmospheric demand on canopy photosynthesis (Chakraborty et al., 2022; Gou et al., 2024), although they partly reflect variation in realized efficiency because the proxy was derived through an LUE formulation. For operational scaling, the practical implication is that tide and radiation should be evaluated jointly. Their statistical contributions cannot be treated as independent when cloud conditions, atmospheric mixing, and tidal phase covary within the available record.

4.3 Cross-platform agreement and scale mismatch

The tower and MODIS series agreed moderately in seasonal rank across 27 matched composite windows (Spearman $\rho = 0.47$, $p = 0.013$; Fig. 8a), and both declined from March to October (Fig. 8b). This correspondence provides a useful magnitude check for the EC-derived proxy, but it is not a validation of the inferred sub-daily process. MODIS did not resolve a tidal-state difference ($p = 0.36$; Fig. 8f), despite the 9.8% contrast in the half-hourly tower record. Eight-day compositing can average observations made under different tidal states, while retrieval uncertainty and the mismatch between a 500-m pixel and the variable EC footprint further weaken direct comparison.

Sentinel-2 supplied finer spatial detail but did not remove the scale problem. Mean FAPAR was lowest in the DEM-defined −0.6 to 0 m sensitivity zone, and the difference from elevated pixels was 44–48% across the three scenes (Cohen's $d = -0.65$ to -0.67;

Figs. 9, 10). FAPAR also increased with elevation more strongly than with distance from mapped tidal channels (r = 0.71–0.79 versus 0.42–0.55; Fig. 10). These patterns are consistent with an inundation gradient, but elevation and channel distance also covary with drainage, salinity, nutrient supply, vegetation structure, and mapping geometry (Gou et al., 2023; Zhu et al., 2021b). The imagery therefore adds spatial context rather than a separate test of the tower-derived threshold.

Nominal pixel counts considerably overstated the information available for spatial inference. Decorrelation distances of approximately 550–800 m reduced the effective sample size to about 24–30 within the 31.9 km² reserve, so pixel-level significance was not interpreted as independent replication (Dutilleul et al., 1993; Meyer & Pebesma, 2021). Vertical uncertainty was even more restrictive: the nominal ±5 m uncertainty of SRTM (Rodríguez et al., 2006; Farr et al., 2007) was much larger than the 0.6 m sensitivity-zone width. The Monte Carlo reduction in detectable area from 19.1% to 3.9% quantified this vulnerability but could not recover sub-metre topography. Agreement among the three platforms should thus be judged by compatible direction and scale, not by treating their observations as equivalent.

4.4 Seasonal spatial associations and model interpretation

The random-forest models described different seasonal allocations of predictor importance (Figs. 11–13). Out-of-bag R^2 declined from 0.807 in spring to 0.692 in summer and recovered to 0.740 in autumn. CO_2 and solar radiation had similar importance in spring, CO_2 ranked first in summer, and solar radiation ranked first in autumn. This reordering is plausible in a monsoon mangrove system where radiation,

https://doi.org/10.5194/egusphere-2026-4707
Preprint. Discussion started: 2 September 2026

atmospheric demand, precipitation, and tidal exchange vary seasonally. It should not, however, be interpreted as a causal partition of controls because SHAP values allocate importance within the fitted predictor set and correlated predictors can exchange importance (Aas et al., 2021; Pei et al., 2022).

The relatively high CO_2 importance illustrates this interpretive problem. Near-surface CO_2 differed between tidal states in the tower record (Fig. 3d), and tidal cycles can influence mangrove stem, soil, and ecosystem carbon exchange (Yong et al., 2024; Zhu et al., 2024). At the spatial resolution used here, CO_2 may also represent atmospheric mixing, ventilation, seasonal meteorology, or covariance with radiation rather than a direct control on canopy absorption. The fitted FAPAR response therefore cannot distinguish a biological CO_2 association from tidal and atmospheric covariation. Vertically resolved CO_2 profiles, turbulence observations, optical FAPAR measurements, and in situ water levels would be required to evaluate these alternatives.

Elevation contributed only about 3–10% of SHAP importance, reaching 9.6% in summer (Fig. 12). Its association with FAPAR was directionally compatible with the tower changepoint, but this agreement was structurally non-independent because elevation defined the spatial zones and entered the landscape model directly. In addition, model performance within the sampled predictor domain does not establish map accuracy in poorly represented environmental conditions (Meyer & Pebesma, 2021; Wadoux et al., 2021). The seasonal models are therefore most useful for identifying hypotheses and measurement priorities. They indicate when radiation, CO_2 covariance, and elevation deserve closer observation, rather than ranking universal controls on

https://doi.org/10.5194/egusphere-2026-4707
Preprint. Discussion started: 2 September 2026

mangrove FAPAR.

4.5 Monitoring implications, limitations, and priorities for validation

The immediate monitoring implication is procedural rather than numerical. Optical acquisitions in intertidal forests should be paired with water level referenced to a local vertical datum, and observations close to a locally estimated transition should be flagged or assigned additional uncertainty. Such screening could reduce the chance that a change in inundation state is mistaken for a change in canopy condition. The −0.3 m threshold and the 0.83 scaling ratio are not transferable constants; they are site calibrations for a low-stature mangrove stand with exposed aerial roots. Other species assemblages, geomorphic settings, and tidal ranges require independent estimation.

The principal limitation is that one site and one partial year cannot establish generality. Tidal height was reconstructed from FES2014 rather than measured at the tower, leaving unquantified classification error near the changepoint. The apparent FAPAR proxy was constrained by EC-derived GPP and a calibrated efficiency term, not by an independent optical instrument, and the same temporal record was used for calibration and evaluation. In the landscape analysis, coarse meteorological fields, uncertain elevation, predictor collinearity, and spatial dependence further limited attribution. These restrictions do not negate the within-record patterns, but they narrow the inference to tide-related sampling risk at Qinglangang.

A decisive validation would combine several measurements that were unavailable here. In situ water levels and local vertical control would test the changepoint directly; optical FAPAR or absorbed-radiation measurements would separate canopy absorption

https://doi.org/10.5194/egusphere-2026-4707
Preprint. Discussion started: 2 September 2026

from realized efficiency; and multi-year observations would permit temporally blocked evaluation of the scaling ratio. Repeated Sentinel-2 acquisitions at contrasting tidal stages, together with UAV, LiDAR, or waterline-constrained elevation models, would improve spatial classification (Shih et al., 2023). Replication across mangrove types would then show whether tidal information improves daily FAPAR and GPP estimates beyond solar geometry and radiation quality alone. Until those tests are available, the workflow is best used as a transparent quality-control framework rather than a universal correction model.

5. Conclusion

Tidal state covaried with an LUE-derived apparent FAPAR proxy at Qinglangang: exposed-period values were 9.8% higher than flooded-period values, and the estimated changepoint occurred near −0.3 m MSL. Across 163 valid days, a site-calibrated instantaneous-to-daily ratio of 0.83 reduced in-sample RMSE by 28% relative to the unity-ratio baseline. This constant ratio did not encode tidal state, and its performance was not evaluated outside the calibration record. MODIS captured part of the seasonal variation but not the tidal contrast, while Sentinel-2 provided only directionally compatible spatial context under substantial elevation and spatial-dependence constraints. The defensible contribution is therefore a workflow for diagnosing tide-related sampling uncertainty, not a transferable tidal correction. Independent optical FAPAR, measured water levels, blocked temporal validation, and replication across mangrove settings are required before the approach can support operational adjustment of satellite observations.

https://doi.org/10.5194/egusphere-2026-4707
Preprint. Discussion started: 2 September 2026

Code availability

The code that support the findings of this study are available from the corresponding author upon request.

Data availability

The data that support the findings of this study are available from the corresponding author upon request

Author Contributions

Demei Zhao: Writing – original draft, Visualization, Software, Methodology, Investigation, Formal analysis. Haolin Chen: Writing – review & editing, Supervision, Methodology, Funding acquisition. Wenmeijun Wang: Writing – review & editing, Methodology, Data curation. Wenhao Huang: Writing – review & editing, Supervision, Methodology. Kangwen Zhu: Funding acquisition, Data curation.

Competing interests

The authors declare that they have no conflict of interest.

Acknowledgments

This work was supported by National Natural Science Foundation of China (42401417), China Postdoctoral Science Foundation Project (2025MD774150), Guangdong Major Project of Basic and Applied Basic Research (2023B0303000017), Shenzhen Science and Technology Program (JCYJ20241202124510015, JCYJ20250604182203005) and GuangDong Basic and Applied Basic Research Foundation (2025A151551008).

References

https://doi.org/10.5194/egusphere-2026-4707
Preprint. Discussion started: 2 September 2026

Aas, K., Jullum, M., & Løland, A. (2021). Explaining individual predictions when features are dependent: More accurate approximations to Shapley values. Artificial Intelligence, 298, 103502. https://doi.org/10.1016/j.artint.2021.103502

Farr, T.G., Rosen, P.A., Caro, E., et al. (2007). The Shuttle Radar Topography Mission. Reviews of Geophysics, 45(2), RG2004. https://doi.org/10.1029/2005RG000183

Chakraborty, T., Lee, X., & Lawrence, D. M. (2022). Diffuse radiation forcing constraints on gross primary productivity and global terrestrial evapotranspiration. Earth's Future, 10(8), e2022EF002805. https://doi.org/10.1029/2022EF002805

Dutilleul, P., Clifford, P., Richardson, S., et al. (1993). Modifying the t test for assessing the correlation between two spatial processes. Biometrics, 49(1), 305–314. https://doi.org/10.2307/2532625

Fratini, G., & Mauder, M. (2014). Towards a consistent eddy-covariance processing: An intercomparison of EddyPro and TK3. Atmospheric Measurement Techniques, 7(7), 2273–2281. https://doi.org/10.5194/amt-7-2273-2014

Friess, D.A., Rogers, K., Lovelock, C.E., et al. (2019). The state of the world's mangrove forests: Past, present, and future. Annual Review of Environment and Resources, 44, 89–115. https://doi.org/10.1146/annurev-environ-101718-033302

Gou, R., Buchmann, N., Chi, J., et al. (2023). Temporal variations of carbon and water fluxes in a subtropical mangrove forest: Insights from a decade-long eddy covariance measurement. Agricultural and Forest Meteorology, 343, 109764. https://doi.org/10.1016/j.agrformet.2023.109764

Gou, R., Chi, J., Liu, J., et al. (2024). Atmospheric water demand constrains net ecosystem production in subtropical mangrove forests. Journal of Hydrology, 630, 130651. https://doi.org/10.1016/j.jhydrol.2024.130651

Gueymard, C.A. (2008). REST2: High-performance solar radiation model for cloudless-sky irradiance, illuminance, and photosynthetically active radiation—Validation with a benchmark dataset. Solar Energy, 82(3), 272–285. https://doi.org/10.1016/j.solener.2007.04.008

Hoerl, A.E., & Kennard, R.W. (1970). Ridge regression: Biased estimation for nonorthogonal problems. Technometrics, 12(1), 55–67. https://doi.org/10.1080/00401706.1970.10488634

https://doi.org/10.5194/egusphere-2026-4707
Preprint. Discussion started: 2 September 2026

Jacquemoud, S., Verhoef, W., Baret, F., et al. (2009). PROSPECT + SAIL models: A review of use for vegetation characterization. Remote Sensing of Environment, 113, S56–S66. https://doi.org/10.1016/j.rse.2008.01.026

Killick, R., Fearnhead, P., & Eckley, I.A. (2012). Optimal detection of changepoints with a linear computational cost. Journal of the American Statistical Association, 107(500), 1590–1598. https://doi.org/10.1080/01621459.2012.737745

Knyazikhin, Y., Martonchik, J.V., Myneni, R.B., et al. (1998). Synergistic algorithm for estimating vegetation canopy leaf area index and fraction of absorbed photosynthetically active radiation from MODIS and MISR data. Journal of Geophysical Research: Atmospheres, 103(D24), 32257–32275. https://doi.org/10.1029/98JD02462

Lloyd, J., & Taylor, J.A. (1994). On the temperature dependence of soil respiration. Functional Ecology, 8(3), 315–323. https://doi.org/10.2307/2389824

Lundberg, S.M., & Lee, S.I. (2017). A unified approach to interpreting model predictions. Advances in Neural Information Processing Systems, 30, 4768–4777.

Lyard, F.H., Allain, D.J., Cancet, M., et al. (2021). FES2014 global ocean tide atlas: Design and performance. Ocean Science, 17(3), 615–649. https://doi.org/10.5194/os-17-615-2021

Mauder, M., Cuntz, M., Drüe, C., et al. (2013). A strategy for quality and uncertainty assessment of long-term eddy-covariance measurements. Agricultural and Forest Meteorology, 169, 122–135. https://doi.org/10.1016/j.agrformet.2012.09.006

Meyer, H., & Pebesma, E. (2021). Predicting into unknown space? Estimating the area of applicability of spatial prediction models. Methods in Ecology and Evolution, 12, 1620–1633. https://doi.org/10.1111/2041-210X.13650

Moncrieff, J.B., Massheder, J.M., de Bruin, H., et al. (1997). A system to measure surface fluxes of momentum, sensible heat, water vapour and carbon dioxide. Journal of Hydrology, 188–189, 589–611. https://doi.org/10.1016/S0022-1694(96)03194-0

Moncrieff, J.B., Clement, R., Finnigan, J., et al. (2004). Averaging, detrending, and filtering of eddy covariance time series. In X. Lee, W. Massman, & B. Law (Eds.), Handbook of Micrometeorology (pp. 7–31). Springer. https://doi.org/10.1007/1-4020-2265-4_2

Monteith, J.L. (1972). Solar radiation and productivity in tropical ecosystems. Journal of Applied

Ecology, 9(3), 747–766. https://doi.org/10.2307/2401901

Monteith, J.L. (1977). Climate and the efficiency of crop production in Britain. Philosophical Transactions of the Royal Society of London. Series B, Biological Sciences, 281(980), 277–294. https://doi.org/10.1098/rstb.1977.0140

Myneni, R., Knyazikhin, Y., & Park, T. (2021). MOD15A2H MODIS/Terra Leaf Area Index/FPAR 8-Day L4 Global 500 m SIN Grid V061. NASA EOSDIS Land Processes DAAC. https://doi.org/10.5067/MODIS/MOD15A2H.061

Nguyen, L. T. M., Hoang, H. T., Choi, E., et al. (2023). Distribution of mangroves with different aerial root morphologies at accretion and erosion sites in Ca Mau Province, Vietnam. Estuarine, Coastal and Shelf Science, 287, 108324. https://doi.org/10.1016/j.ecss.2023.108324

Papale, D., Reichstein, M., Aubinet, M., et al. (2006). Towards a standardized processing of net ecosystem exchange measured with eddy covariance technique: Algorithms and uncertainty estimation. Biogeosciences, 3(4), 571–583. https://doi.org/10.5194/bg-3-571-2006

Pebesma, E.J. (2004). Multivariable geostatistics in S: The gstat package. Computers & Geosciences, 30(7), 683–691. https://doi.org/10.1016/j.cageo.2004.03.012

Pei, Y., Dong, J., Zhang, Y., et al. (2022). Evolution of light use efficiency models: Improvement, uncertainties, and implications. Agricultural and Forest Meteorology, 317, 108905. https://doi.org/10.1016/j.agrformet.2022.108905

Rani, V., Schwing, P. T., Jayachandran, P. R., et al. (2023). Carbon stocks and sequestration rate in mangroves and its major influencing factors from highly urbanised port city, southern India. Journal of Environmental Management, 335, 117542. https://doi.org/10.1016/j.jenvman.2023.117542

Reichstein, M., Falge, E., Baldocchi, D.D., et al. (2005). On the separation of net ecosystem exchange into assimilation and ecosystem respiration: Review and improved algorithm. Global Change Biology, 11(9), 1424–1439. https://doi.org/10.1111/j.1365-2486.2005.001002.x

Rodríguez, E., Morris, C.S., & Belz, J.E. (2006). A global assessment of the SRTM performance. Photogrammetric Engineering & Remote Sensing, 72(3), 249–260. https://doi.org/10.14358/PERS.72.3.249

Shih, S.-S., Hsu, W.-C., & Hsu, Y.-W. (2023). Waterline digital elevation model development to

https://doi.org/10.5194/egusphere-2026-4707
Preprint. Discussion started: 2 September 2026

quantify inundation duration and coastal protection of tidal wetlands. Science of the Total Environment, 874, 162519. https://doi.org/10.1016/j.scitotenv.2023.162519

Spitters, C.J.T., Toussaint, H.A.J.M., & Goudriaan, J. (1986). Separating the diffuse and direct component of global radiation and its implications for modeling canopy photosynthesis. Part I. Components of incoming radiation. Agricultural and Forest Meteorology, 38(1–3), 217–229. https://doi.org/10.1016/0168-1923(86)90060-2

Sun, Z., An, Y., Kong, J., et al. (2024). Exploring the spatio-temporal patterns of global mangrove gross primary production and quantifying the factors affecting its estimation, 1996–2020. Science of the Total Environment, 908, 168262. https://doi.org/10.1016/j.scitotenv.2023.168262

Wadoux, A. M. J.-C., Heuvelink, G. B. M., de Bruin, S., et al. (2021). Spatial cross-validation is not the right way to evaluate map accuracy. Ecological Modelling, 457, 109692. https://doi.org/10.1016/j.ecolmodel.2021.109692

Webb, E.K., Pearman, G.I., & Leuning, R. (1980). Correction of flux measurements for density effects due to heat and water vapour transfer. Quarterly Journal of the Royal Meteorological Society, 106(447), 85–100. https://doi.org/10.1002/qj.49710644707

Wilczak, J.M., Oncley, S.P., & Stage, S.A. (2001). Sonic anemometer tilt correction algorithms. Boundary-Layer Meteorology, 99(1), 127–150. https://doi.org/10.1023/A:1018966204465

Wright, M.N., & Ziegler, A. (2017). ranger: A fast implementation of random forests for high dimensional data in C++ and R. Journal of Statistical Software, 77(1), 1–17. https://doi.org/10.18637/jss.v077.i01

Wutzler, T., Lucas-Moffat, A., Migliavacca, M., et al. (2018). Basic and extensible post-processing of eddy covariance flux data with REddyProc. Biogeosciences, 15(16), 5015–5030. https://doi.org/10.5194/bg-15-5015-2018

Yong, Z.-J., Lin, W.-J., Lin, C.-W., et al. (2024). Tidal influence on carbon dioxide and methane fluxes from tree stems and soils in mangrove forests. Biogeosciences, 21, 5247–5260. https://doi.org/10.5194/bg-21-5247-2024

Zhang, N.R., & Siegmund, D.O. (2007). A modified Bayes information criterion with applications to the analysis of comparative genomic hybridization data. Biometrics, 63(1), 22–32.

https://doi.org/10.5194/egusphere-2026-4707
Preprint. Discussion started: 2 September 2026

https://doi.org/10.1111/j.1541-0420.2006.00662.x

Zhang, Y., Hu, Z., Wang, J., et al. (2023). Temporal upscaling of MODIS instantaneous FAPAR improves forest gross primary productivity (GPP) simulation. International Journal of Applied Earth Observation and Geoinformation, 121, 103360. https://doi.org/10.1016/j.jag.2023.103360

Zheng, Y., & Takeuchi, W. (2022). Estimating mangrove forest gross primary production by quantifying environmental stressors in the coastal area. Scientific Reports, 12, 2238. https://doi.org/10.1038/s41598-022-06231-6

Zhu, X., Chen, J., Li, L., et al. (2024). Asynchronous methane and carbon dioxide fluxes drive temporal variability of mangrove blue carbon sequestration. Geophysical Research Letters, 51, e2023GL107235. https://doi.org/10.1029/2023GL107235

Zhu, X., Qin, Z., & Song, L. (2021a). How land-sea interaction of tidal and sea breeze activity affect mangrove net ecosystem exchange? Journal of Geophysical Research: Atmospheres, 126(8), e2020JD034047. https://doi.org/10.1029/2020JD034047

Zhu, X., Sun, C., & Qin, Z. (2021b). Drought-induced salinity enhancement weakens mangrove greenhouse gas cycling. Journal of Geophysical Research: Biogeosciences, 126(8), e2021JG006416. https://doi.org/10.1029/2021JG006416

Zhu, X., Hou, Y., Zhang, Y., et al. (2021c). Potential of sun-induced chlorophyll fluorescence for indicating mangrove canopy photosynthesis. Journal of Geophysical Research: Biogeosciences, 126(4), e2020JG006159. https://doi.org/10.1029/2020JG006159